Amplitude and phase control of a coherent superposition of degenerate states. II. Experiment

Frank Vewinger,* Manfred Heinz,† Ulrich Schneider,‡ Christian Barthel,§ and Klaas Bergmann‖
Fachbereich Physik der Technischen Universität Kaiserslautern, Erwin-Schrödinger-Straße, 67653 Kaiserslautern, Germany
(Received 15 November 2006; published 25 April 2007)

We present experimental demonstrations of a technique, based on multistate variants of the stimulated Raman adiabatic passage (STIRAP) process, that allows efficient and robust preparation of a preselected superposition of two or three degenerate states (magnetic sublevels of an atom) and the measurement of their relative amplitudes and phases. The experiments verify theoretical results described in the preceding paper. We perform our experiments with neon atoms in a supersonic beam: atoms in the metastable $^3P_0$ state are transferred to a superposition of the metastable $^3P_2$ magnetic sublevels, using four different linkage patterns. Because the preparation utilizes adiabatic passage, it is robust against small fluctuations of the Rabi frequencies and temporal shape of the coupling fields. The relative phases and the amplitude ratios of the components of the prepared superpositions are experimentally analyzed using a technique termed phase-to-population mapping. Phase-to-population mapping is based on laser-induced fluorescence after the atoms have undergone optical pumping cycles induced by an additional laser. The optical pumping process maps the superposition phases into populations of a subset of levels by means of a filtering laser field, and is robust against variations in the intensity and detuning of that field.

DOI: 10.1103/PhysRevA.75.043407 PACS number(s): 32.80.Qk, 03.65.Vf, 03.67.Hk

I. INTRODUCTION

In a companion paper [1], we presented theoretical details of techniques that allow the preparation, and subsequent characterization of coherent superpositions of magnetic sublevels, applicable to atoms in an atomic beam. The preparation techniques are based on generalizations of the stimulated Raman adiabatic passage (STIRAP) technique [2,3], while the detection is based on a technique termed phase-to-population mapping [1,4,5], which is an extension of earlier theoretical proposals [6].

As a substantial extension to already published results [4,5] we here show the feasibility of our proposals in a proof-of-principle experiment using a stream of identically prepared metastable neon atoms. Starting from the initial state $^3P_0$ we create two- or three-state superpositions within the Zeeman manifold of the $^3P_2$ level using two coupling laser fields, called P and S laser. We present measurements for four different coupling schemes, which show that the parameters of the superposition are determined completely by the coupling laser fields. We determine the parameters of the prepared superposition using the coupling between the levels $^3P_2$ and $^3P_1$ induced by an additional laser field. When the population remaining after the interaction, or the fluorescence from the state $^3P_1$ [6], is determined as the laser field polarization is changed the parameters of the superposition can be determined. Alternative measurement schemes have been shown experimentally, e.g., Hanle resonances [7] and Stern-Gerlach-type measurements [8] have been used to determine angular momentum distributions.

In Sec. II, we describe the experimental apparatus used in the experiment and the means to control the parameters of the prepared superposition. In Sec. III, we present the results obtained for four different coupling schemes. Two of the schemes, twin STIRAP and tripod STIRAP, allow the preparation of a two-state superposition with arbitrary amplitude ratios and phases. The third one, extended tripod STIRAP, prepares a three-state superposition. Because only two controllable parameters exist in this coupling scheme, the relative phases between the three components of the superposition cannot be controlled independently. This is remedied by the fourth coupling scheme, extended diamond STIRAP, that introduces an additional laser field and thus two additional control parameters. This allows the independent control of the relative phases and the amplitude ratios of the prepared superposition. Additionally, this coupling scheme exhibits quantum interference effects from two competing pathways that connect the initial state with one of the superposition components. Because of the interference, the population of this state depends on the phases of the coupling laser fields.

II. APPARATUS

In this section, we describe the setup of our experiment. First, we detail the source of metastable neon atoms, and then describe the typical configuration of the interacting lasers. We finish with a description of the experimental parameters that are changed to control the properties of the coherent superposition.

*Present address: Institut für Angewandte Physik, Wegelerstraße 8, 53115 Bonn, Germany. Electronic address: vewinger@iap.uni-bonn.de
†Present address: AMD Fab36 LLC & Co. KG, Wilschdorfer Landstraße 101, 01109 Dresden, Germany.
‡Present address: Institut für Physik, Johannes Gutenberg-Universität, Staudingerweg 7, 55128 Mainz, Germany.
§Present address: Department of Physics, Harvard University, Cambridge, MA 02138, USA.
‖Electronic address: bergmann@rhrk.uni-kl.de

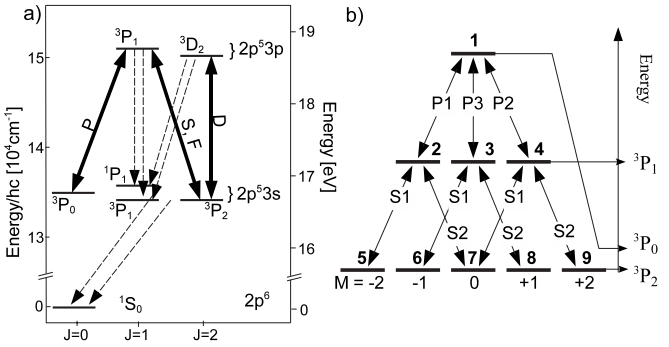

FIG. 1. (a) The energetic levels and laser couplings used in the experiment. (b) The numbering of the levels and the couplings used throughout the text. Note that the level $^3P_0$ was shifted energetically to the uppermost position to make the couplings clearer.

A. Main setup

The neon atoms for the experiment emerge from a water-cooled cold-cathode discharge nozzle source [9,10] operated at a pressure of about 10 mbar and placed inside a differentially pumped vacuum chamber. The background pressure is $\approx 10^{-4}$ mbar in the chamber that hosts the discharge source. The stream of atoms is formed into a beam by a skimmer, after which they move into a second pumping stage where the pressure is 10^{-6} mbar. The atoms finally reach the experimental chamber with a pressure on the order of $\approx 10^{-9}$–10^{-8} mbar, which is separated from the second pumping stage using a 50 cm long tube with diameter of 1 cm. The mean flow velocity of the atomic beam is $v_{flow} \approx 800$ ms^{-1}, with a full width at half maximum of about $\Delta v \approx 300$ ms^{-1}. To ensure that the Doppler width orthogonal to the flow direction is smaller than the natural linewidth the beam is collimated using a 1 mm diameter skimmer and a 50 μm $\times$ 3 mm slit positioned 183 cm apart. This results in a strongly elongated elliptical beam profile.

A fraction of the atoms, of the order of 10^{-4} [11], is in the metastable states $^3P_0$ or $^3P_2$ of the $2p^5\,3s$ electronic configuration. Prior to arrival in the interaction region of the P and S lasers the population of the $^3P_2$ level of the ^{20}Ne isotope is depleted by optical pumping: A preparation laser excites the atoms in the metastable level $^3P_2$ to the $^3D_2$ level of the $2p^5\,3p$ configuration from where the atoms decay either back to the $^3P_2$ level or to the short-lived $^3P_1$ and $^1P_1$ levels of the $2p^5\,3s$ configuration followed by the emission of a vacuum ultraviolet (vuv) photon (74 nm) as the atoms return to the $^1S_0$ ground state (see Fig. 1 for an energy-level scheme). Because the interaction time of the atoms with the preparation laser is much longer than the lifetime of the upper excited level, and the magnetic field is not compensated in this region, all atoms are eventually removed from the metastable $^3P_2$ state prior to their interaction with the P and S lasers. Figure 2 shows the beam geometry.

After the preparation stage the collimated beam enters the main interaction region where the superposition is prepared and probed. For the preparation, it passes, at right angles, through the centers of the P and S laser, which couple the transition $^3P_0 \leftrightarrow {}^3P_1$ and $^3P_1 \leftrightarrow {}^3P_2$, respectively. The direction of the S-laser propagation defines the quantization axis

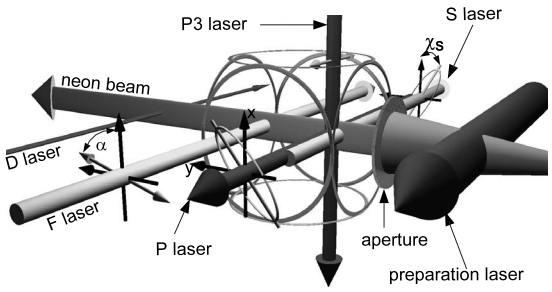

FIG. 2. Geometric arrangement of the atomic beam (neon) and the P and S lasers as well as the filter laser and the detection laser used for the phase measurement. The P laser is either propagating parallel to the S laser (denoted by P laser), or perpendicular (denoted by $P3$ laser) with its linear polarization pointing in $\hat{\mathbf{z}}$ direction defined by the S-laser axis. In the former case, the P laser induces couplings denoted by $P1$ and $P2$ in Fig. 1. The angle χ_S (χ_P) gives the direction of the main axis of the S-laser (P-laser) polarization ellipse with respect to the x axis. The filter laser is linearly polarized at an adjustable angle α with respect to the x axis. The preparation laser is used for the preparation of the initial state $^3P_0$ in front of the beam shaping aperture.

$\hat{\mathbf{z}}$, and the $\hat{y}$ direction is taken as the propagation direction of the atomic beam. The P laser is either propagating in the $\hat{\mathbf{z}}$ direction, coupling $\Delta M = \pm 1$ transitions, or in the $\hat{x}$ direction, coupling only the $\Delta M = 0$ transition. In the latter case, it is linearly polarized, with the direction of polarization pointing in $\hat{\mathbf{z}}$ direction. Both beams have a diameter of 2.5 mm and the P laser is typically offset 2–3 mm downstream the S laser, resulting in a counterintuitive pulse sequence. After the interaction, the atoms are in a superposition of the form

$$\Psi(t) = \sum_{n=5}^{9} A_n \exp(i\varphi_n)\psi_n(t), \quad t > t_f, \tag{1}$$

where $\psi_n(t)$ are the bare atomic basis states in the rotating frame [1]. The phases φ_n depend only on the phase of the coupling P and S laser, while the positive amplitudes A_n depend on their polarization. This superposition is defined with respect to a quantization axis that is parallel to the direction of the S laser.

Another 2 cm further downstream, the beam passes through the F-laser beam, of diameter 3 mm, whose linear polarization forms an angle α with the x axis. The F laser is resonant on the $^3P_2 \leftrightarrow {}^3P_1$ transition, and thus it removes the population within the Zeeman states $6'$–$8'$, where the prime denotes states defined with respect to a quantization axis parallel to the polarization of the F laser [1]. The population remaining in level $^3P_2$ after the interaction with the F laser can be written using rotation matrices $d^J_{2,M}$ as [1,12]

$$S(\alpha) = 2 \sum_{M<\tilde{M}} [1 + (-1)^{M+\tilde{M}}] d^J_{2,M}\left(\frac{\pi}{2}\right) d^J_{2,\tilde{M}}\left(\frac{\pi}{2}\right) A_M A_{\tilde{M}} \times \cos[\alpha(\tilde{M} - M) + (\varphi_M - \varphi_{\tilde{M}})] + 2\sum_M [d^J_{2,M}(\pi/2)]^2 A_M^2, \tag{2}$$

where the indices M and $\tilde{M}$ run over all Zeeman states of the $J=2$ level. The signal $S(\alpha)$ contains an oscillating term depending on α. This dependence allows the determination of the relative phases φ_n and the amplitudes A_n of the initial superposition, Eq. (1). The angle α is changed using a half-wave plate in the F beam, which is rotated by a stepper motor with 1600 steps for a full revolution.

In the special case with the F laser propagating parallel to the S laser, considered here, not all phases can be determined unambiguously. This can be remedied by using other directions and ellipticities for the F laser [13].

In the interaction region between the S- and P-laser interaction and the F laser, the Earth's magnetic field and stray magnetic fields are actively compensated to a level ≤ 0.5 μT by three pairs of external coils in Helmholtz arrangement. The bandwidth of the servo loop is 1 kHz, which is adequate to compensate time varying homogeneous fields from nearby power supplies. Because the field is negligible the magnetic sublevels remain degenerate and do not undergo Larmor precession, which would lead to a redistribution within the created superposition.

Some 450 mm further downstream from the F laser, the atoms pass, at right angle, through the D-laser beam directly underneath a channeltron detector that monitors the vuv fluorescence $\mathcal{F}(\alpha)$ resulting from a cascaded decay of the excited $^3D_2$ level, which is proportional to the population in the $^3P_2$ level. This resulting fluorescence signal can be written as $\mathcal{F}(\alpha)=\eta S(\alpha)$, where η is the detection efficiency, and $S(\alpha)$ is given by Eq. (2). During the flight along the 450 mm long path between the F and D lasers, the atoms are exposed to an inhomogeneous magnetic field with nonuniform directions resulting from the Earth's magnetic field and the time varying field of nearby electrical devices. This magnetic field induces Larmor precessions that mix the Zeeman sublevels. Because the width of the velocity distribution is approximately $\Delta v \approx 0.35 v_{flow}$ and the atoms undergo of the order of 100 Larmor cycles, the population remaining in the $^3P_2$ level after the optical pumping with the F laser is uniformly distributed among the five magnetic sublevels. Thus the fluorescence induced by the D laser from any one of the sublevels is proportional to the population remaining after the filter process, independent of the D laser polarization. The diameter of the D laser is ≈ 0.5 mm, and thus a factor of 5 smaller than that of the S and P lasers. Therefore, the D-laser probes atoms which have experienced a more or less uniform S- and P-laser pulse area. We normalize the fluorescence signal to the count rate with the F laser blocked, thereby obtaining directly the detection efficiency η. This allows us to determine the signal $S(\alpha)$ from the measured fluorescence $\mathcal{F}(\alpha)$.

Three independent continuous single mode dye lasers are used in this experiment. All laser beams are delivered to the apparatus by single mode fibers. The state of polarization is controlled by fiber polarizers at the fiber exits followed by Glan-Taylor prisms. One of the dye lasers provides the S- and F-laser radiation, the power of a second one is shared by the D laser and the laser used for the preparation of the initial state $^3P_0$, while the third dye laser supplies the P radiation.

B. Controlling the parameters of the superposition state

Because the S laser propagates along the quantization axis, its Rabi frequency can be expressed in the helicity basis as

$$\hat{e}_S\Omega_S = \hat{e}_+\Omega_{S1} + \hat{e}_-\Omega_{S2}e^{-2i\chi_S} \tag{3}$$

$$= \Omega_S[\hat{e}_+ \cos\epsilon_S + \hat{e}_- \sin\epsilon_S e^{-2i\chi_S}], \tag{4}$$

where the amplitude ratio $\tan\epsilon_S$ is connected with the ellipticity $\omega=\epsilon_S-\pi/4$. When the P laser propagates parallel to the S laser, it can be written in the helicity basis, yielding

$$\hat{e}_P\Omega_P = \hat{e}_+\Omega_{P1} + \hat{e}_-\Omega_{P2}e^{-2i\chi_P} \tag{5}$$

$$= \Omega_P[\hat{e}_+ \cos\epsilon_P + \hat{e}_- \sin\epsilon_P e^{-2i\chi_P}]. \tag{6}$$

In the case where the P laser propagates perpendicular to the S laser, with its linear polarization pointing in the $\hat{\mathbf{z}}$ direction, it induces couplings denoted with $P3$ in Fig. 1. In this case it can be expressed by

$$\hat{e}_P\Omega_P = \hat{e}_z\Omega_P. \tag{7}$$

The relative phase χ_i $(i=S,P)$ and the amplitude ratio $\tan\epsilon_i$ can be varied experimentally by inserting quarter- and half-wave plates into the P- or S-laser beam. The half-wave plate rotates the main axis of polarization ellipse by twice its rotation angle, $\chi_i=2\theta_{\lambda/2}$. Because the relative phases of the superposition are determined by the relative phase of the laser fields a half-wave plate allows the control of the phase of the prepared superposition.

A quarter-wave plate within the P- or S-laser beam rotates the main axis of the polarization ellipse by $\chi_i=\theta_{\lambda/4}$ $(i=P,S)$. Additionally, it changes the ellipticity of the light field, and thus the amplitude ratio $\tan\epsilon_i$. This allows control of the amplitudes A_n of the superposition state, which depend on the Rabi frequencies of the coupling fields and thus on their relative amplitudes.

A combination of quarter- and half-wave plates allows the full control of the polarization state, and thus the independent control of ϵ_i and χ_i. This yields four controllable parameters, which is sufficient to fully control a three state superposition determined by two relative phases and two amplitude ratios. To prepare superpositions consisting of four or five Zeeman levels an additional linearly polarized S field propagating along the $\hat{x}$ direction would need to be introduced. Because this field has a wave vector pointing in a different direction than the one of the original S field, this will lead to a spatially periodic phase pattern, with a periodicity given by the wavelength of the S laser. This cannot be realized in a beam experiment, as the different phases cannot be measured independently due to the limited spatial resolution. This restriction does not apply to atoms that are spatially confined to $\Delta r \ll \lambda$, e.g., in a trap.

III. RESULTS AND DISCUSSION

In the following, we present and discuss results obtained for the four coupling schemes presented in [1]. We prepare a

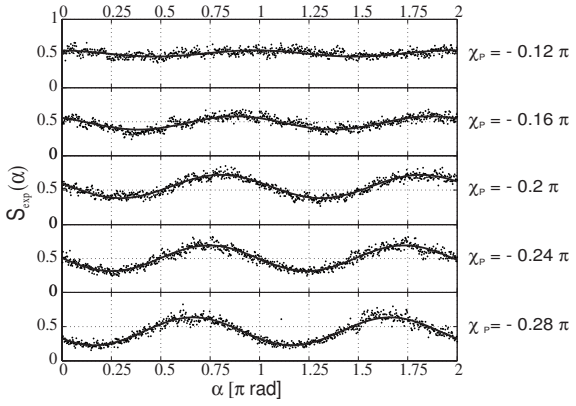

FIG. 3. Population measured by fluorescence induced by the *D* laser after optical pumping as a function of the *F*-laser polarization angle α for coherent superposition states Ψ_{twin} [see Eq. (8)] with different relative phase χ_P and amplitude ratio tan ϵ. For this experiment, we have $\epsilon+\pi/4=2\chi_P$. Individual frames are for different choices of χ_P, as given in the graph. The solid line is a cosine fit whose phase yields the relative phase of the superposition.

superposition state with known amplitudes A_n and phases φ_n through experimental control of the polarization of the lasers. We retrieve these amplitudes and phases through an independent experiment and establish the reliability of the method by comparison of the preset and measured parameters. Where needed, we mention changes in the laser setup as compared to Fig. 2.

With twin STIRAP chosen as an example, we compare measured and calculated results for different phases and amplitude ratios, showing the results gained using phase-to-population mapping and comparing these to the theoretically expected data. With tripod STIRAP chosen as an example, we discuss the influence of magnetic fields on the superposition states. Finally, the experiments involving extended tripod STIRAP and extended diamond STIRAP demonstrate that the phase of a three-component superposition can be controlled and measured. For all four examples, we report selected results on the experimentally measured phases and the amplitude ratio. The dependence on the laser parameters, as well as the influence of magnetic fields, is considered.

We compare our measured results to density matrices obtained by numerically integrating the master equation including the states 1–9, together with a state 10 which serves as a reservoir state for the decay outside the system, resulting from population in states 2–4. The dissipation operator Γ is used in the form given in [4,14], as this speeds up the computation time compared to using the full Lindblad operators [15].

A. Twin STIRAP

The superposition created when we have nonzero coupling for *P*1, *P*2, and *S*2, see Fig. 1, has contributions of levels 7 and 9. It is given by

$$\Psi_{\text{twin}}(t) = \frac{1}{\mathcal{N}}[\cos \epsilon_P \psi_7 + \sqrt{6} \sin \epsilon_P e^{(+i2\chi_P)} \psi_9], \tag{8}$$

where tan ϵ_P is the amplitude ratio between the two helicity components of the *P* laser (see Sec. II B). As can be seen, the

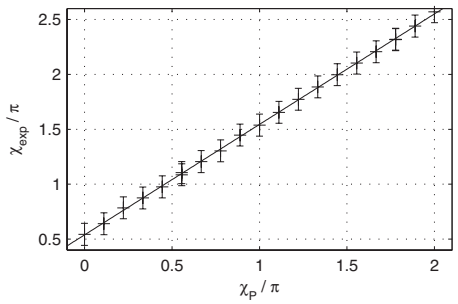

FIG. 4. Measured phase χ_{exp} versus the phase χ_P of the *P* laser. This phase is controlled by the angle of polarization of the *P* laser by a $\lambda/2$ plate. The straight line is a linear function with a slope of unity. The offset between χ_{exp} and χ_P is due to a small uncompensated magnetic field component along the quantization axis. The error bars result from the inclusion of the fluctuations in the neon source.

superposition is solely determined by the two parameters ϵ_P and χ_P.

The experimental setup for the preparation of the superposition given by Eq. (8) is similar to the one shown in Fig. 2, with a circularly polarized *S*-laser beam, and the *P* laser propagating parallel to *S*, thus $\Omega_{S1}=\Omega_{P3}=0$. With the propagation direction of the *S* laser taken as the quantization axis, this implements the twin STIRAP coupling scheme. The polarization of the *P* laser can be changed by means of a half-wave and a quarter-wave plate, allowing the control of the superposition parameters.

Inserting the amplitudes and phases of the superposition (8) into Eq. (2) yields the expected population $S(\alpha)$ measured with the *D* laser. It reads

$$S(\alpha) = \frac{1}{24}\{36 \cos^2 \epsilon_P + \sin^2 \epsilon_P + 12 \cos \epsilon_P \sin \epsilon_P \cos[2(\alpha + \chi_P)]\}. \tag{9}$$

It is solely determined by the phase χ_P and the amplitude ratio tan ϵ_P of the *P* laser.

Figure 3 shows typical data for the signal $S(\alpha)$ as a function of the *F*-laser polarization angle α for several choices of the amplitude ratio tan ϵ and angle χ_P, set by a quarter-wave plate within the *P* beam. The data points have been fitted by a function of the form $f(\alpha)=a \cos[2(\alpha+\chi_{exp})]-b$ to retrieve the relative phase χ_{exp} and the amplitude ratio tan ϵ_{exp}, which are compared to the preset values χ_P and tan ϵ_P.

Several observations can be made from Fig. 3. First of all, the variation of the signal $S(\alpha)$ with α can be observed as predicted by Eq. (9). The phase of the modulation depends on the phase of the *P* laser, as is expected. Second, the modulation depth of the curves depends on the amplitude ratio tan ϵ_P. Both observations confirm the expected behavior. Figure 4 shows the variation of the phase χ_{exp} extracted from the fitted curves with the relative phase χ_P of the *P* laser. From Eqs. (8) and (9), we expect

$$\chi_{exp} = \chi_P. \tag{10}$$

The linear relation with a slope of unity is clearly confirmed. The offset between χ and χ_P is due to an uncompensated

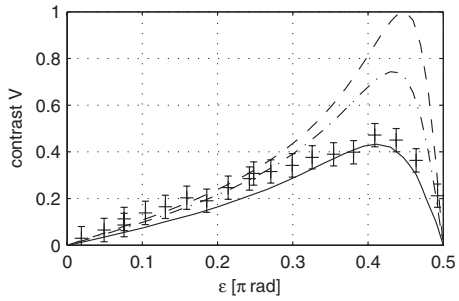

FIG. 5. The measured contrast as a function of the amplitude ratio $\tan \epsilon$ of the P laser. The dashed line is the contrast expected from Eq. (12). The dash-dotted line shows a simulation including spontaneous emission during the filter process, and the solid line includes spontaneous emission as well as a small magnetic field of 0.5 μT in $\hat{\mathbf{z}}$ direction. The experimentally determined contrast shows the characteristic structure of the simulation. The error bars are determined from the statistical distribution of the measured data.

magnetic field along the quantization axis, which leads to an additional constant phase shift. This will be detailed in Sec. IV. The measurements confirm that we are able to control the phase of the prepared superposition, and measure this parameter using the phase-to-population mapping method. The amplitudes of the superposition can also be controlled, as can be seen by considering the contrast of the curves shown in Fig. 3.

The contrast of the curve is defined as

$$V = \frac{\max[S(\alpha)] - \min[S(\alpha)]}{\max[S(\alpha)] + \min[S(\alpha)]}. \tag{11}$$

For the case of a superposition prepared using twin STIRAP, Eq. (8), it reads

$$V(\epsilon_P) = \frac{12 \sin(2\epsilon_P)}{37 + 35 \cos(2\epsilon_P)}. \tag{12}$$

Figure 5 shows the contrast extracted from the measured curves (Fig. 3), together with a curve following Eq. (8) and the results of a numerical simulation. It is evident that the contrast V is always smaller than one. The experimental data follow qualitatively the theoretically expected variation with ϵ_P. A comparison with the numerical simulation shows good agreement, from which we conclude that spontaneous emission is the limiting process: During the interaction with the F laser about 9% of the population pumped to the $^3P_1$ level decays back to the $M=\pm 2$ states of $^3P_2$. Thus, additional population is added to this levels during the F-laser interaction. In our numerical simulations, we account for this additional population. A second mechanism, included in the simulation, leads to a change of the contrast: Small residual magnetic fields ($B_{res} \leq 0.5\ \mu T$) lead to an accumulation of a (velocity dependent) phase difference between M states or induce Larmor precession between the Zeeman states. The consequences of Larmor precession are discussed in Sec. IV.

The good agreement between the experimental data and the simulation shows that the amplitudes of the superposition can be controlled using the ellipticity of the P laser. The amplitude is measured using phase-to-population mapping if the spontaneous emission during the filtering process by the F laser is accounted for. As the oscillator strength for the different neon transitions are known [16], this can be done, thus giving access to both the phase and the population distribution of the prepared superposition.

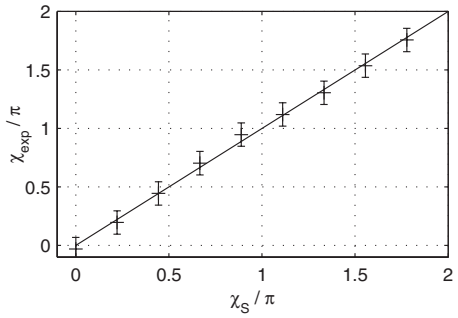

FIG. 6. Measured phase χ_{exp} versus the phase χ_S of the S laser, controlled by means of a $\lambda/2$ plate (see Sec. II B). The straight line is a linear fit with a slope of unity and an axis cut of zero.

B. Tripod STIRAP

The tripod coupling [17] is realized for nonzero values of $P3$, $S1$, and $S2$, see Fig. 1. It couples state 1 to the states 6 and 8, preparing a superposition of the form

$$\Psi_{\text{tripod}}(t) = [\cos \epsilon_S \psi_6 + \sin \epsilon_S e^{(-i2\chi_S)} \psi_8], \tag{13}$$

where $\tan \epsilon_S$ is the amplitude ratio between the two helicity components of the S laser. For the preparation of the superposition given in Eq. (13), we use the setup shown in Fig. 2, where the linearly polarized P laser propagates in x direction, perpendicular to the S and F laser. Its direction of polarization is parallel to the quantization axis $\hat{\mathbf{z}}$, thereby inducing transitions with $\Delta M = 0$. The polarization of the S laser is changed by means of a half-wave and a quarter-wave plate, allowing full control of the relative phase and the relative amplitudes of the prepared superposition.

As for twin STIRAP, we measure $S(\alpha)$ as a function of the angle α of the F-laser polarization and extract the relative phase and the amplitude ratio of the superposition. For a superposition of the form (13), we expect the variation of the signal $S(\alpha)$ with α, ϵ_S, and χ_S to be

$$S(\alpha) = \frac{1}{2}[1 + 2 \cos \epsilon_S \sin \epsilon_S \cos 2(\alpha + \chi_S)]. \tag{14}$$

We extract the parameters by fitting a function of the form $f(\alpha) = a \cos 2[\alpha + \chi] - b$ to the experimental data. As the phase is fully determined by the phase of the S laser we expect

$$\chi_{exp} = \chi_S. \tag{15}$$

Figure 6 shows the measured phase χ_{exp} as a function of the S laser phase χ_S. Since the linear fit reveals a slope of unity, the measured phase is, within the experimental uncertainty, the same as the phase imprinted by the S laser. For this experiment, the ambient magnetic field was carefully compensated to avoid additional phases induced by magnetic

fields (see Sec. IV), thus no offset is observed for $\chi_S=0$. Evaluation of the contrast as a function of the ellipticity (not shown) reveals also that the amplitude ratio of the superposition is determined by the amplitude ratio $\tan \epsilon_S$ of the S laser. Thus, as in the case of twin STIRAP, the parameters of the superposition are fully determined by the laser polarization, in this case of the S laser.

C. Extended tripod STIRAP

The extended tripod STIRAP coupling with nonzero coupling for $P1$, $S1$, and $S2$ (see Fig. 1) allows the preparation of a superposition of the three Zeeman levels (levels 5, 7, and 9), which is characterized by two amplitude ratios and two relative phases. The coupling scheme does not allow the independent control of the relative phases and the amplitude ratios since a change of the relative phase between the field $S1$ and $S2$ affects the relative phase between states 5 and 7 or 7 and 9 alike. Furthermore, the amplitude ratio of the two helicity components of the S laser determine the two relative amplitudes of the final superposition. Full control of the relative phases and amplitude ratios requires the addition of a field $P2$ which couples states 1 and 4, as is detailed in Sec. III D.

Using the extended tripod coupling scheme we obtain a superposition of the form

$$\Psi_{\text{xtri}} = \frac{1}{\mathcal{N}}[A_5\psi_5 + A_7 e^{i2\chi_S}\psi_7 + a_9 e^{i4\chi_S}\psi_9]. \tag{16}$$

The coefficients A_n are given by

$$A_5 = \frac{1}{6}\cos\epsilon_S(7 - 5\cos 2\epsilon_S), \tag{17}$$

$$A_7 = \frac{2}{3}\sin^2\epsilon_S, \tag{18}$$

$$A_9 = \frac{1}{3}\cos\epsilon_S \sin^2\epsilon_S. \tag{19}$$

Both the phase between states 5 and 7 as well as the phase between 7 and 9 is fully determined by χ_S, thus an independent control is not possible in this scheme. The expected signal $S(\alpha)$, Eq. (2) can be written as

$$S(\alpha,\chi) = \frac{1}{8}[A_5^2 + 6A_7^2 + A_9^2] + \frac{\sqrt{6}}{4}A_7(A_5 + A_9)\cos(2\chi + 2\alpha) + A_5A_9\cos(4\chi + 4\alpha). \tag{20}$$

The third term, oscillating with 4α, is caused by the contribution of state 9 with twice the phase difference relative to state 5, as compared to state 7. The dominant term of Eq. (20) is proportional to the amplitudes A_5 and A_7; the population that reaches state 9 is less than 2% of the total population in the $^3P_2$ level for any value of ϵ_S. Because of this, we neglect the term oscillating with 4α in our analysis. This does not influence the measurement of the phase, as the maximum of the curve $S(\alpha)$ remains at the same position.

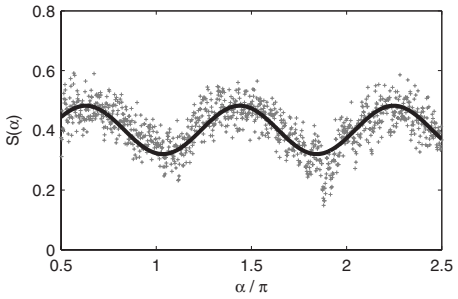

FIG. 7. Signal $S(\alpha)$ obtained for a superposition prepared using extended tripod STIRAP. The S laser is linear polarized, thus the two helicity components are equal, $\Omega_{S1}=\Omega_{S2}$.

Figure 7 shows the experimental signal $S(\alpha)$, together with a fit function of the form $f(\alpha)=a\cos 2[\alpha+\chi]-b$. The good agreement between the fit and the measured data justifies the neglect of the $\cos 4\alpha$ term. The measured data are the raw data obtained by the channeltron detector. The scatter of the data points is due to fluctuations of the flux of neon, which is in the order of 10%. As we measure 1600 points per experimental run, our fit averages over these fluctuations.

The phase χ_{exp} extracted from the fits is plotted in Fig. 8 as a function of the phase χ_S of the S laser. Equation (20) shows that again the measured phase is connected to the laser phase by

$$\chi_{exp} = \chi_S. \tag{21}$$

This is confirmed by the experimental data, which follow this function. The good agreement between the experimental data and the expected behavior confirms the fact that we can control the phases of a three state superposition. The control of the amplitude ratio is also possible (not shown). We give an example of this control in the following section on the example of extended diamond STIRAP.

D. Extended diamond STIRAP

The extended diamond scheme allows the preparation of a three-state superposition, where the four parameters describ-

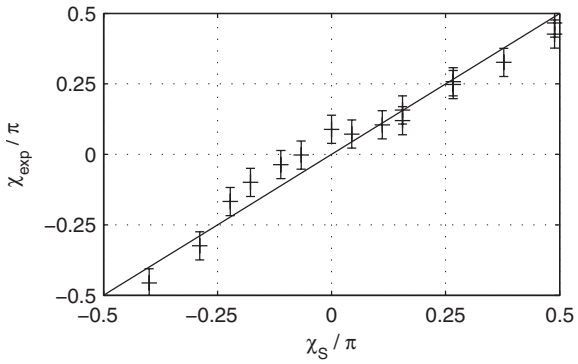

FIG. 8. Measured phase χ_{exp} versus the phase χ_S of the S laser. The phase χ_S is controlled by the angle of polarization of the S laser by means of a $\lambda/4$ plate. The straight line is the function $\chi_{\text{exp}}=\chi_S$. The error bars result from the inclusion of fluctuations in the neon flux.

ing the superposition are fully controlled by the polarization of the coupling laser fields. For the coupling shown in Fig. 1, the prepared superposition after the adiabatic transfer has the form

$$\Psi(t) = e^{-i\omega_S t}[A_5(t_f)\psi_5 + A_7(t_f)\psi_7 + A_9(t_f)\psi_9], \quad (22)$$

where the coefficients at time $t \to t_f$ are given by

$$A_5 = \frac{1}{\sqrt{3}\mathcal{N}}\cos\epsilon_S[e^{-2i\chi_P}\cos\epsilon_P \sin\epsilon_P \cos\epsilon_S - e^{-2i\chi}\sin\epsilon_S(\sin^2\epsilon_P + 2\sin^2\epsilon_S)],$$

$$A_7 = \frac{\sqrt{2}}{\mathcal{N}}[\cos^2\epsilon_P \sin^2\epsilon_S + \cos^2\epsilon_P(2\sin^2\epsilon_S + \sin^2\epsilon_P)],$$

$$A_9 = \frac{1}{\sqrt{3}\mathcal{N}}\sin\epsilon_S[-e^{2i\chi_S}\cos\epsilon_S(\cos^2\epsilon_P + 2\cos^2\epsilon_S) + e^{2i\chi_P}\cos\epsilon_P \sin\epsilon_P \sin\epsilon_S]. \quad (23)$$

Here, the coefficient $1/\mathcal{N}$ is a normalization factor. As state 7 can be reached by two different pathways, namely 1-2-7 and 1-4-7, interferences between these pathways can occur. These manifest in the dependence of the populations on the laser phases. In the case of a linear polarized S and P field, and thus $\epsilon_S = \epsilon_P = \pi/4$, the populations are given by

$$P_5 = -\frac{2a^2\sin^2(\chi_S - \chi_P)}{-2(a^2+b^2) + 2a^2\cos 2(\chi_S - \chi_P)}, \quad (24)$$

$$P_7 = \frac{b^2}{a^2 + b^2 - a^2\cos 2(\chi_S - \chi_P)}, \quad (25)$$

$$P_9 = -\frac{2a^2\sin^2(\chi_S - \chi_P)}{-2(a^2+b^2) + 2a^2\cos 2(\chi_S - \chi_P)}. \quad (26)$$

The expected signature of interference is evident from the oscillatory dependence on the laser phases χ_S and χ_P.

We focus in this case on the interference that manifests in the populations, and modify the setup to directly measure the population in either level 7 or the levels 5 and 9. After the interaction of the atoms with the S- and P-laser beams the detection laser (diameter 3 mm) illuminates the atomic beam at right angle 10 mm downstream from the P laser, with its linear polarization aligned with the quantization axis $\hat{\mathbf{z}}$. The laser frequency is chosen to couple the transition $^3P_2 \to {}^3P_1$ or, alternatively, the transition $^3P_2 \to {}^3D_2$. In the former case, all population in the states 6–8 is removed by optical pumping, while in the latter case, optical pumping removes the states 5, 6, 8, and 9, leaving only the population in state 7. A fraction of the population pumped into the upper state decays back into the $^3P_2$ level, from where it is either removed in subsequent pumping cycles or leads to additional population of the uncoupled states. As the coupling strength for all involved transitions are known, the final population in the magnetic sublevels can be calculated numerically or can be approximated using rate equations to describe the optical pumping. In the latter case, coherences between the ground states are ignored. In this rate, equation approximation the measured populations P_i^{meas} can be written as

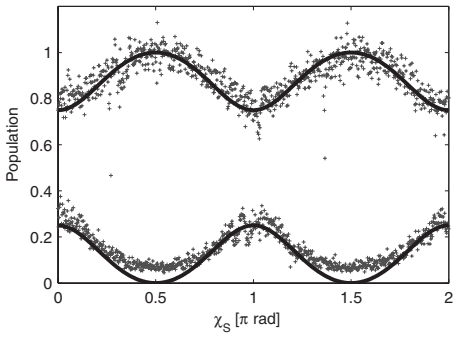

FIG. 9. Population in the states 7 (lower curve) and the sum of the populations in states 5 and 9 (upper curve), as a function of the phase χ_S. The solid curves show the signal expected from Eq. (27).

$$P_7^{meas} = \frac{1 - 0.029}{4}\cos^2(\chi_S - \chi_P) + 0.029, \quad (27)$$

$$(P_5 + P_9)^{meas} = \frac{1 - 0.017}{4}\sin^2(\chi_S - \chi_P) + 0.754. \quad (28)$$

Here, the numerical values are derived using the following procedure: The population is optically pumped to the upper states 2 to 4, from where it either decays out of the system or back to states 5 to 9. Repeating this cycle of optical pumping followed by spontaneous emission leads to the steady-state populations given in Eq. (27). The obtained curve deviates less than 1% from the curve obtained by a numerical solution of the Liouville equation.

Typical experimental results for the population in the states 5, 7, and 9 is shown in Fig. 9 as a function of the phase χ_S, with a fixed phase $\chi_P = 0$. The variance of the data points is given by statistical fluctuations in the flux of neon atoms, while the "mavericks" around 0.25 and 1.3 are due to short term fluctuations in the laser frequency, causing a two-photon detuning, thus decreasing the transfer efficiency. Both curves show the expected oscillating behavior given in Eq. (24). The solutions given in Eq. (27) are shown for comparison in the plot as solid lines. They show a qualitatively good agreement with both the population in states 7 and 5 + 9. The population in state 7 shows a discrepancy with the analytical curve near its minima, which can be explained by two mechanisms, both of which lead to an increase in the population in state 7. First, frequency fluctuations in the S and P fields result in an imperfect population transfer, leaving some population in states orthogonal to the dark state (22) due to diabatic coupling. Second, the states 6 and 8 receive some population due to Larmor precession. To minimize the consequences of the magnetic fields, we actively compensated these in the region between the S, P lasers and the F laser, as described in Sec. II A, using three pairs of external coils in Helmholtz arrangement. Neither effect can be quantified, because we do not have sufficiently precise values for either the magnetic field within the interaction region or the amount of diabatic coupling. Nonetheless, the data show the quantum

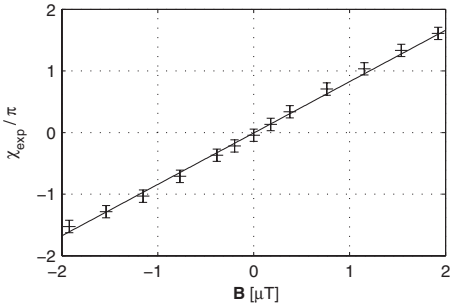

FIG. 10. Measured phase χ_{exp} versus the applied magnetic field in quantization direction for a fixed phase χ_S. The solid line is a linear fit with a slope of $0.83\pi/\mu$T.

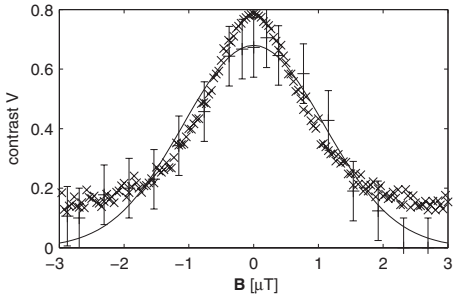

FIG. 11. Measured contrast $V(B)$ versus the applied magnetic field parallel to the quantization axis. The solid line is a Gaussian fit according to Eq. (32), and the crosses (×) result from a Monte Carlo simulation. The error of the measured contrast is derived from the statistical fluctuations of $S(\alpha,\chi)$.

interference between the two given excitation pathways for the state 7, leading to the oscillatory behavior in the population of the magnetic sublevels of the $^3P_2$ level.

IV. INFLUENCE OF MAGNETIC FIELDS

Using the example of tripod STIRAP, we discuss the influence of magnetic fields on the prepared superposition. We apply a small magnetic field along the quantization axis $\hat{\mathbf{z}}$, and measure the relative phase as well as the contrast as a function of the magnetic field for a fixed S laser phase χ_S. When the atoms are exposed to a magnetic field for a duration $\Delta\tau$, they accumulate an additional phase given by

$$\gamma_B = M\omega_L(B)\Delta\tau = M\frac{g\mu_B}{\hbar}\Delta\tau B_\parallel. \tag{29}$$

Here, g is the Landé g factor, μ_B is the Bohr magneton, $B_\parallel$ is the magnetic field strength, and $\omega_L(B)=g\mu_B B_\parallel/\hbar$ is the Larmor frequency. After the interaction with the magnetic field, the relative phase of the components of the superposition, Eq. (13) changes to

$$\Phi_{tripod}(t\to\infty)\to\cos\epsilon\psi_6+\sin\epsilon e^{-i2(\chi_S+\gamma_B)}\psi_8. \tag{30}$$

Thus, the measured phase should vary linearly with the applied magnetic field. The measured phases are shown in Fig. 10, together with a linear fit. From this fit, we derive that $\gamma_B/B_\parallel=0.83\pi/\mu$T. Using the known parameters of our Helmholtz coils in Eq. (29) we expect $\gamma_B=(0.86\pm0.05)\pi/\mu$T, showing a good agreement with the value retrieved from the measured data. Magnetic fields thus can be used to additionally control the relative phase between the components of the prepared superposition, but due to the velocity distribution this will lead to an ensemble-averaged phase, i.e., the phase of a random atom selected out of the beam has a range of possible values. This can be clearly seen when the contrast of the measured curves is evaluated.

The width Δv of the velocity distribution $f(v)$ of the atoms in the beam ($v=800$ m/s, $\Delta v/v=0.35$) leads to a variation of the duration of the interaction time. Thus, a distribution of phases is expected after the atoms have traveled through the magnetic field and the ensemble average of Eq. (30) evolves towards an incoherent superposition of states 6 and 8. The ensemble-averaged signal S_B is given by

$$S_B(\alpha)=\int S(\alpha,\chi+\gamma_B)f(v)dv. \tag{31}$$

The experimentally determined velocity distribution can be approximated by a Gaussian distribution with a width T_0 centered around T_{flight}. In this case, it is straightforward to show that the contrast V varies with the magnetic field $B_\parallel$ as

$$V(B)=V_0\exp\{[-\omega_L(B)T_0]^2\}, \tag{32}$$

where V_0 is the contrast observed for $B=0$. Figure 11 shows the measured contrast $V(B)$ together with a Gaussian fit and the results of a Monte Carlo simulation based on the solution of the full Liouville equation including the velocity distribution and the spontaneous emission induced by the interaction with the F laser. The good agreement of experiment and simulation confirms that the distribution of the interaction time of the atoms with the magnetic fields are the main source of the loss of coherence. Obviously it is important to maintain good control of the magnetic field in the interaction region if the atoms (or molecules) in the given state have a nonvanishing magnetic moment.

V. SUMMARY

We have presented a method which allows the preparation of a superposition of degenerate quantum states with two or three components with a well-defined phase. Furthermore, we have demonstrated a scheme for the measurement of the relative phase between the components as well as the ratio of amplitudes. In particular, the twin STIRAP and tripod STIRAP coupling schemes allow the preparation of an arbitrary but well-defined superposition state of two magnetic sublevels. Extended diamond STIRAP can be utilized to prepare superpositions of three states, with arbitrary phases and amplitudes of the components. Both the two- and three-state superpositions are characterized using phase-to-population mapping. Our analysis shows that the inclusion of spontaneous emission is essential in modeling the detection of the amplitudes, while the retrieved phases are exact if this emission is omitted in the modeling.

The detection techniques discussed in this work are relevant, quite generally, to measure the superposition phase in a stream of identical systems prepared by any technique. The method discussed here allows a high degree of flexibility and carries significant potential for the manipulation and observation of quantum states where phase control is crucial.

ACKNOWLEDGMENTS

This work has been supported by the Deutsche Forschungsgemeinschaft. The authors thank B. W. Shore for valuable discussions and assistance in the preparation of the manuscript. This work was supported by the Marie-Curie Training Network EMALI of the EU.

[1] F. Vewinger, M. Heinz, B. W. Shore, and K. Bergmann, preceding paper, Phys. Rev. A **75**, 043406 (2007).
[2] K. Bergmann, H. Theuer, and B. W. Shore, Rev. Mod. Phys. **70**, 1003 (1998).
[3] N. V. Vitanov, T. Halfmann, B. W. Shore, and K. Bergmann, Annu. Rev. Phys. Chem. **52**, 763 (2001); N. V. Vitanov, M. Fleischhauer, B. W. Shore, and K. Bergmann, Adv. At., Mol., Opt. Phys. **46**, 55 (2001).
[4] M. Heinz, F. Vewinger, U. Schneider, L. P. Yatsenko, and K. Bergmann, Opt. Commun. **264**, 248 (2006).
[5] F. Vewinger, M. Heinz, R. Garcia-Fernandez, N. V. Vitanov, and K. Bergmann, Phys. Rev. Lett. **91**, 213001 (2003).
[6] N. V. Vitanov, B. W. Shore, R. G. Unanyan, and K. Bergmann, Opt. Commun. **179**, 73 (1999); N. V. Vitanov, J. Phys. B **33**, 2333 (2000).
[7] V. Milner and Y. Prior, Phys. Rev. A **59**, R1738 (1999).
[8] G. Klose, G. Smith, and P. S. Jessen, Phys. Rev. Lett. **86**, 4721 (2001).
[9] *Atomic and Molecular Beam Methods*, edited by G. Scoles (Oxford University Press, Oxford, 1988).
[10] H. Hotop, in *Experimental Methods in the Physical Sciences* (Academic, New York, 1996), Vol. 29B, Chap. 11, pp. 191–215.
[11] H. Hotop, J. Lorenzen, and A. Zastrow, J. Electron Spectrosc. Relat. Phenom. **23**, 347 (1981).
[12] R. N. Zare, *Angular Momentum: Understanding Spatial Aspects in Chemistry and Physics* (Wiley, New York, 1988).
[13] P. Ivanov and N. V. Vitanov, Opt. Commun. **264**, 368 (2006); C. Barthel, Z. Kis, U. Schneider, and K. Bergmann (unpublished).
[14] B. W. Shore, *The Theory of Coherent Atomic Excitation* (Wiley, New York, 1990).
[15] R. Kosloff, M. A. Ratner, and W. B. Davis, J. Chem. Phys. **106**, 7036 (1997).
[16] P. Hartmetz and H. Schmoranzer, Phys. Lett. **93A**, 405 (1983); P. Hartmetz and H. Schmoranzer, Z. Phys. A **317**, 1 (1984); S. Inatsugu and J. R. Holmes, Phys. Rev. A **11**, 26 (1975).
[17] R. G. Unanyan, B. W. Shore, and K. Bergmann, Phys. Rev. A **63**, 043401 (2001); R. G. Unanyan, K. Bergmann, and B. W. Shore, *ibid.* **59**, 2910 (1999).